encit 2020

ABCM Associação Brasileira de Engenharia e Ciências Mecânicas

18th Brazilian Congress of Thermal Sciences and Engineering
November 16–20, 2020 (Online)

ENC-2020-0452
CFD ANALYSIS OF THE INSTALLATION EFFECT ON A TRUCK'S GENERIC SIDE-VIEW MIRROR

Eduardo de Oliveira Carvalho
Aeronautics Institute of Technology (ITA)
Praça Marechal Eduardo Gomes, 50 - Vila das Acacias, São José dos Campos - SP, 12228-900
eduardoc@ita.br

André Fernando de Castro da Silva
Aeronautics Institute of Technology (ITA)
Praça Marechal Eduardo Gomes, 50 - Vila das Acacias, São José dos Campos - SP, 12228-900
andref@ita.br

Abstract. *Transportation is one of the human activities that most consumes natural resources. Freight by truck is a cornerstone of this process, and they typically suffer from aerodynamic inefficiency. Of all truck components, side-view mirrors remain to have substantial aerodynamic relevance. Past studies point out that they contribute with 3-6% of the truck's total drag. Characterized by the presence of a strong wake, the flow interaction between truck and mirror plays a fundamental role in making the flow past a side-view mirror complex. A proper investigation about how the presence of the cabin interferes in the flow-field on the side of the truck can shed light on some methodological questions. In particular, the issue of when simplified mirror-only experimental/simulation data can be used to make inferences about the performance of installed mirror. Such knowledge would allow experiments/simulations of lower cost to be used to study certain aspects of the flow. This work seeks to achieve this by simulating a two-dimensional version of the flow past side-view mirrors with and without the installation effect and comparing its impacts. Furthermore, reliable flow information is obtained through the use of Unsteady Reynolds-Averaged Navier-Stokes (URANS) simulations and analysed with the Spectral Proper Orthogonal Decomposition (SPOD) technique. Even though the results highlight some degree of similarity in how the vortex shedding relates to the instantaneous drag in both cases, the time-averaged drag coefficient turns out to be considerably higher in the presence of the installation effect. Furthermore, the SPOD modes are considerably different when considering the installation effect, indicating more complexity in the existing time-coherent flow structures and even the addition of new ones.*

Keywords: *Truck Aerodynamics, Side-View Mirror, Installation Effect, CFD, SPOD*

1. INTRODUCTION

With today's globalized production and trade, long-distance freight transport represents a key feature to the manufacturing of almost every day-to-day product. Besides the relevance in all kinds of production scale, freight transport also is responsible for the consumption of a considerable amount of the world's energy. Estimations from the International Energy Agency (IEA, 2019) pointed out that 28.9% of the world's total energy in 2017 was consumed by the transport sector. This impact is even more substantial for specific countries, like Brazil. Owning the fifth-largest territory and its freight predominantly made by roads, Brazil has a transport sector accountable for 37.3% of the national energy consumption in 2017 (IEA, 2019).

Corresponding to 61.1% of Brazil's total freight (CNT, 2018), road transport is known to be more inefficient when compared to rails or watercraft. In spite of the high costs of maintenance of the vehicles and infrastructure (Rodrigue *et al.*, 2013), 80% of the total energy spent on domestic transportation in developed countries in 2010 was employed on road transport (Gao *et al.*, 2015). In the Brazilian case, this number reached 93.5% in 2016 (EPE, 2019), evidencing the country's dependency on this mode of transport. Estimations reveal that the Brazilian truck fleet is growing and currently has about 2 million vehicles (SINDIPEÇAS and ABIPEÇAS, 2019; IBPT and Empresômetro, 2018). This category of vehicles is dominant on the rental freight market, trucks represent approximately 89% of all 1,449,485 self-propelled vehicles employed in the sector (ANTT, 2020). The average fleet age in the sector is around 14 years, but in some specific contexts, they can get even older. For instance, simple trucks belonging to autonomous drivers have an averaged age of 25 years (ANTT, 2020). The large number of drivers and the profound dependency on truck freight made Brazilian

economic balance very sensitive to fuel prices. The advanced average age of these vehicles indicates a general difficulty in fleet renewal. Given these conditions, a more viable way of addressing cost issues would be by increasing fuel efficiency through geometrical improvements to relatively inexpensive components.

Due to their frontal area, trucks can be considered as bluff bodies. This kind of design faces a large amount of air resistance, mainly associated with pressure drag. This can be so substantial that some trucks travelling at 83 km/h can use up to 40% of their fuel to overcome air resistance (Frank and Turney, 2016). However, a typical truck design can attain 20-30% of drag reduction by acquiring specific aerodynamic enhancements (Raut *et al.*, 2015; Roy and Srinivasan, 2000). Smith *et al.* (2007) mention that, within the industry, there is a good acceptance of 2-3% drag reduction correlating to a lowering of approximately 1% of fuel consumption.

Although truck models generally have great potential for aerodynamic improvements, these solutions are hindered by operational and economic limitations (Cooper, 2004). Besides targeting drag reduction, design solutions also have to take into account application cost and operational viability in order to attain significant industrial acceptance. Also, it is worthy noting that these limitations change from place to place as they depend on the local environment and vehicular regulation.

Due to local legislation, truck manufacturers have to conceive different designs. In both Europe and Brazil, traffic law constrains the maximum value of the total length of the semi-truck hitched to the trailer. Therefore, in order to to maximize cargo, people and companies tend to purchase models with the cabin placed on top of the engine (CoE - cabin over engine). Because of the flatter front, the CoE configuration suffers from an aerodynamic disadvantage in comparison to the conventional cabin (Hjelm and Bergqvist, 2009). The need for a more compact cabin also limits the range of possible aerodynamic enhancements in its shape design.

Left with limited options to improve the cabin's aerodynamics, designers have to focus on improvements to components whose shape can significantly interfere in the truck's total drag. Out of these components, the side-view mirror stands outs as a relevant target of these enhancements. As the literature indicates (Bayraktar *et al.*, 2004; Smith *et al.*, 2007; Raut *et al.*, 2015), these mirrors can be accountable for 3-6% of the truck's total drag. Table 1 summarizes literature data on side-view mirrors' drag. Since drag can considerably vary from one model of mirror to another, there is substantial space for design enhancement of this component (Cresswell and Hertz, 1992; Smith *et al.*, 2007). Furthermore, the complexity of the problem is highlighted by the flow interactions between the mirror and its nearby components, like the cabin's A-pillar. This interplay is known as the installation effect (IE) (Yao *et al.*, 2018).

Table 1: Data about the side-view mirrors' drag in literature. Mirror's drag impact represents the percentage ratio between the mirrors' and the trucks' drag. Installation effect refers to whether the analysis considered or not the presence of the truck's cabin during the acquirement of the data of the mirror's drag. Reproduced from Carvalho and da Silva (2021).

Model Name	**Mirror's Drag Impact**	**Simulation or Experiment**	**Installation Effect**	**Bibliographic Source**
Standard Mirror	8.5%	Experiment	No	Cresswell and Hertz (1992)
Teardrop-shaped Mirror	10%	Experiment	No	Cresswell and Hertz (1992)
Fully-faired Mirror	5.3%	Experiment	No	Cresswell and Hertz (1992)
Freightliner's Aerodynamic Mirror	4.5%	Experiment	Yes	Smith *et al.* (2007)
Freightliner's Aerodynamic Mirror	5.8%	Simulation	Yes	Smith *et al.* (2007)
Not Specified	4.6%	Simulation	Yes	Bayraktar *et al.* (2004)
Not Specified	3.2%	Simulation	Yes	Raut *et al.* (2015)

Since the real extension of the impacts of the IE to a side-view mirror is not well known, deeper investigations are required. This work seeks to obtain further information on how the A-pillar interferes with the flow past a generic-shape side-view mirror. The purpose is to evaluate whether this effect can be neglected by comparing a mirror-only (MO) and a IE simulation.

2. Geometric Model

In order to develop a realistic analysis, the geometry employed in this work was inspired by a commercial product, the Bepo's W-910 model. The two-dimensional version of the employed geometry is displayed by Fig. 1a. Shape simplifications include the use of a flat reflective surface installed directly on the rear face, without the protective lateral edges of the mirror's housing. The mirror's housing lateral face that is most distanced from the external wall is called external side. Its counterpart close to the wall is denominated internal side. The reflective surface is called rear face and its opposite is named front face. In addition to the shape, positioning also interferes in the physics of the problem. To properly characterize a realist mirror's positioning, two rotation axes were considered: one to move the bracket, represented by θ, and another to rotate the mirror's housing, represented by α. The bracket rotates around the the Cartesian system's origin. Besides θ, this movement also depends on the bracket's length R_S. The mirror's housing does not rotate around its geometric center, instead, it moves in respect to an axis whose position is defined by L_L and E. The dimensions and

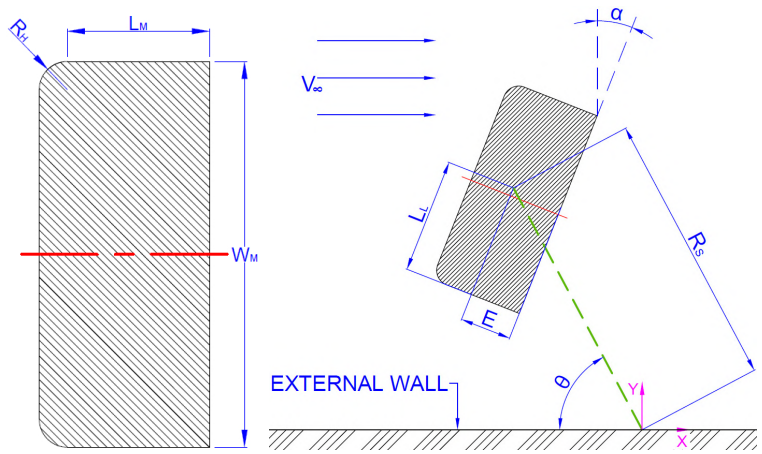

(a) (b)

Figure 1: (a) Geometric dimensions of the two-dimensional mirror. (b) Positioning dimensions of the mirror. Reproduced from Carvalho and da Silva (2021).

the orientation system employed are displayed in Figure 1b.

With all dimensions set, the orientation angles were calculated implementing the legislative requirements of the truck's side-view mirror as criteria. In Brazilian legislation, specifically the item 5.2.1 of the appendix III of resolution 703/2017 of the National Transit Council (CONATRAN), every class II mirror needs to provide a specific field of vision given by transverse and longitudinal distances. The transverse distance is measured from the vehicle most prominent point to the most external point in the field of view provided by the mirror. The longitudinal distance is evaluated from the x position of the driver's eyes to a specific point behind him/her. To attain to the regulation, the driver's field vision needs to contemplate 1 and 5 meters of transverse distance for 4 and 30 meters of longitudinal distance, respectively. Besides the mirror's position, this calculation requires the location of the driver's eyes. Considering that the two globes are aligned in y direction and separated by a distance E_d, their position is given by the x distance a and y distance b from the midpoint between eyes and the bracket's axis. Finally, from the set of angles that meet these requirements, the chosen ones were $\alpha = 21.5°$ and $\theta = 62°$. All numeric values used to define the body's dimensions and positioning are present in Tab. 2.

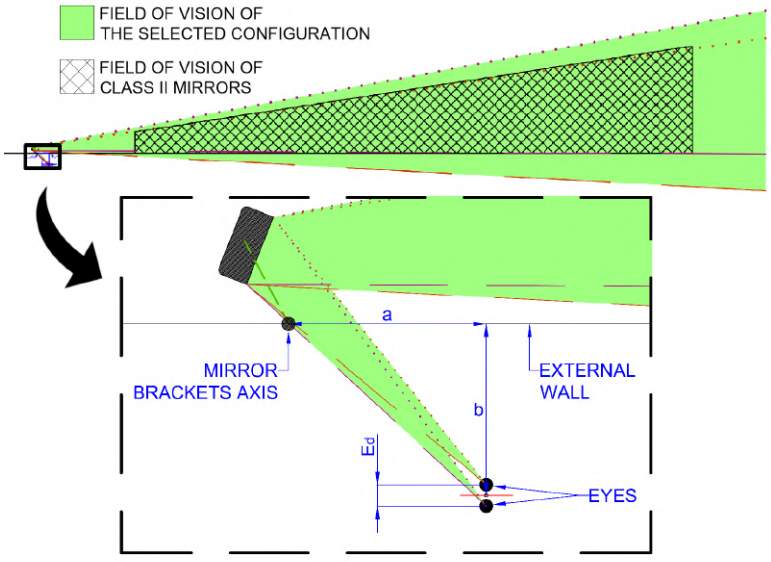

Figure 2: Legally-required field of vision for a side-view mirror in the proposed conditions. Reproduced from Carvalho and da Silva (2021).

In order to analyze the installation effect, another geometric model was constructed. Aiming at achieving a reasonable computational cost while still allowing for a initial perspective on the installation effect, the second model was designed to reproduce the cabin's front, without the rear end. The front face width W_T and the distance between the mirror's support axis and the cabin front face L_{TF} were estimated from the Volkswagen Constellation 19,320. Those dimensions were incorporated into the proportions of the Ground Transport System (GTS) used by Manosalvas-Kjono *et al.* (2014). The

Table 2: Numeric values for the mirror's dimensions (left), the bracket positioning variables (middle) and the proportions employed in the field of vision (right). Adapted from Carvalho and da Silva (2021).

Geometric Variable	Values [mm]	Geometric Variable	Values [mm]	Geometric Variable	Values [mm]
R_H	16	R_S	284	a	604
L_M	81	L_L	119	b	523
W_M	220	E	53	E_d	65

truck's sidewall length L_{NS} was considered to be long enough to reduce mesh costs while not substantially interfering at the mirror's body forces. Figure 3 shows the final layout of this geometry and Tab. 3 reveals its values.

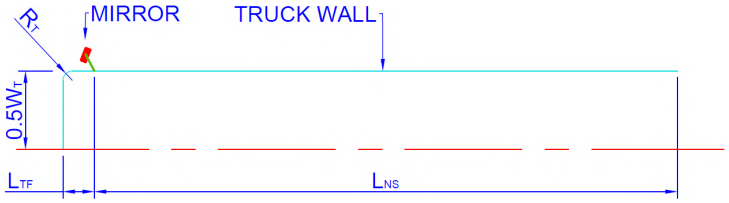

Figure 3: Geometry employed to reproduce the installation effect cut by a symmetry plane.

Table 3: Values of the dimensions employed to reproduce a simplified truck's cabin.

Geometric Variable	Values [mm]
W_T	2,362
R_T	140.6
L_{TF}	474.3
L_{NS}	8,816

3. Methodology

3.1 Flow Properties and Solver

The velocity magnitude chosen to reproduce ordinary cruise conditions was of 22.2 m/s ($\approx$ 80 km/h). In combination with another flow/geometric variables, this velocity represented a Reynolds number of 3.35×10^5 and a Mach number of 0.0652. A flow past a bluff body with a high Reynolds number is typically associated with a detached flow substantially composed of turbulent structures.

All simulations were run using the Stanford University Unstructured (SU2) code. It is an open-source suite of CFD tools and aerodynamic shape design (Palacios *et al.*, 2013). Because of the prohibitively expensive computational costs of the Direct Numerical Simulation (DNS) and Large Eddy Simulation (LES) approaches, the Unsteady Reynolds-Averaged Navier-Stokes (URANS) method was the one selected for this work. To close its equations, a Shear Stress Transport (SST) turbulence model was applied. Developed by Menter (1994), this model balances the use of $k-\epsilon$ and $k-\omega$ through a blending function. This is performed by the SST mainly using the $k-\omega$ in the near wall zones and primarily using the $k-\epsilon$ relatively far from the body, in wake regions (Pope, 2000; Menter, 1994). This way, each method is applied in regions where it can more accurately reproduce the turbulence's effects. As a drawback, the SST model is not properly capable of predicting the turbulent transition during the drag crisis of bluff bodies (Yuce and Kareem, 2016).

As for the discretization method, the Jameson-Schmidt-Turkel (JST) numerical scheme was selected (Jameson *et al.*, 1981). The combination of URANS with SST and JST was previously tested by Manosalvas-Kjono *et al.* (2014). The authors concluded that it provided a satisfactory equilibrium of computational cost and accuracy for the analysis of design of heavy-vehicles. A second-order dual time-stepping scheme was used to undertake the unsteady simulations.

3.2 Two-dimensional Mesh

With a substantial level of complexity, a good first approach to simulate the flow past a side-view mirror is to perform it in two-dimensions. When compared to its 3D counterpart, the 2D simulation allows initial results to be collected with less computational effort and occupying less memory storage. As it is usually the case for high-Reynolds RANS simulations, three-dimensional meshes usually require up to $10^6 - 10^7$ nodes, while the two-dimensional ones commonly demand $10^4 - 10^5$. Due to unsteadiness of the problem, the final cost is then scaled by the multiples snapshots, resulting in a

difference of computational expenses of one or two orders of magnitude.

Moreover, the two-dimensional simulation can give information about where to expect flow detachment, wake's size and behaviour and boundary layer evolution. For instance, two-dimensional meshes can be implemented to estimate the level of refinement required for boundary layer cells. This is a critical aspect to satisfy the $y^+ < 1$ criterion and properly capture boundary layer flow. This information can be later used to accelerate to the process of constructing a 3D mesh and performing the corresponding simulation.

To simulate the side-view mirror without the presence of the cabin, the chosen MO mesh domain was designed as having a flat external wall. This mesh was built using the mirror's housing height as reference ($H_W = 480mm$) and its geometry is shown in Fig 4. Its is composed of a rectangle attached to a quarter of an ellipse. The far-field boundary condition was selected to the inlet, sides, and outlet of the mesh and no-slip wall at all mirror's surfaces. To reproduce wind tunnel flow characteristics at a reasonable computational cost, a slip wall boundary condition was set at the external wall.

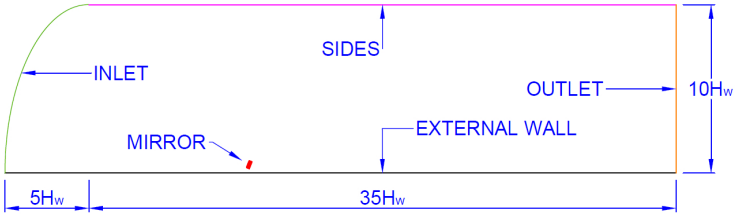

Figure 4: The dimensions and names of the boundary conditions employed in the MO mesh. Reproduced from Carvalho and da Silva (2021).

The final version of this mesh was constructed using 101,786 points and 161,763 elements. The boundary layer segment was generated employing quadrilateral elements in a structured fashion. Other segments were created using unstructured mesh with triangular elements.

The IE mesh domain size was based on the truck's width, as Fig. 5 shows, and has two extra boundary conditions. The first new boundary condition was the symmetry plane inserted in the form of a longitudinal straight line upstream of the truck. The second one was the no-slip condition on the truck walls.

The truck side wall ends in with the dimensions mentioned in Fig. 3, connected to this same line is again the external wall with slip condition.

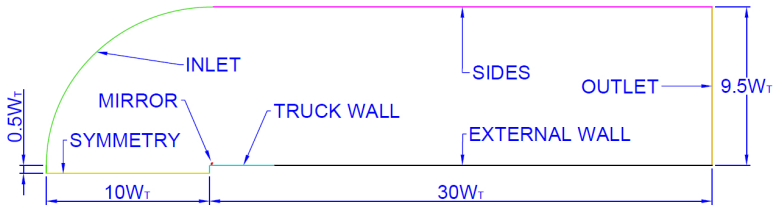

Figure 5: Domain and boundary conditions of the mesh used to investigate the installation effect.

The IE mesh was generated with 180,144 points and 257,146 interior elements. The method applied to the treatment of boundary layer elements was the same used in the previous mesh. To prevent solution errors in the region where the truck wall ends and the external wall begins, a transition region was constructed. Between this two parts there is a transition mesh ensuring a smooth change in elements size.

Both meshes are shown by Fig. 4, the different refinement zones can be seen in their full domain pictures in the first line of the image. The other lines shows with more the details the near-body region.

3.3 Spectral Proper Orthogonal Decomposition

Complex phenomena, like the ones associated with detached flows, usually displays multiple structures (or patterns) developing at different timescales. A better understanding of the main flow mechanisms can be achieved through the breakdown of these events. This kind of analysis allows targeted investigations, focusing on structures that directly influence variables of interest, like drag. This kind of analysis can be performed by employing the Spectral Proper Orthogonal Decomposition (SPOD). This method breaks complex periodic data into modes that are perfectly correlated to these structures. Each one of these modes is also uncorrelated to events of other modes (Towne *et al.*, 2018).

The SPOD requires a data set composed of sequential discrete-time snapshots. To be properly performed, the employed data set needs to satisfy two frequency-related conditions. The first one is that the sampling frequency has to be high enough to capture the highest frequency of interest (Nyquist criterion). The second is about the lowest frequency of interest and the total number of snapshots (resolution criterion). Since the SPOD relies on the Welch's method to achieve

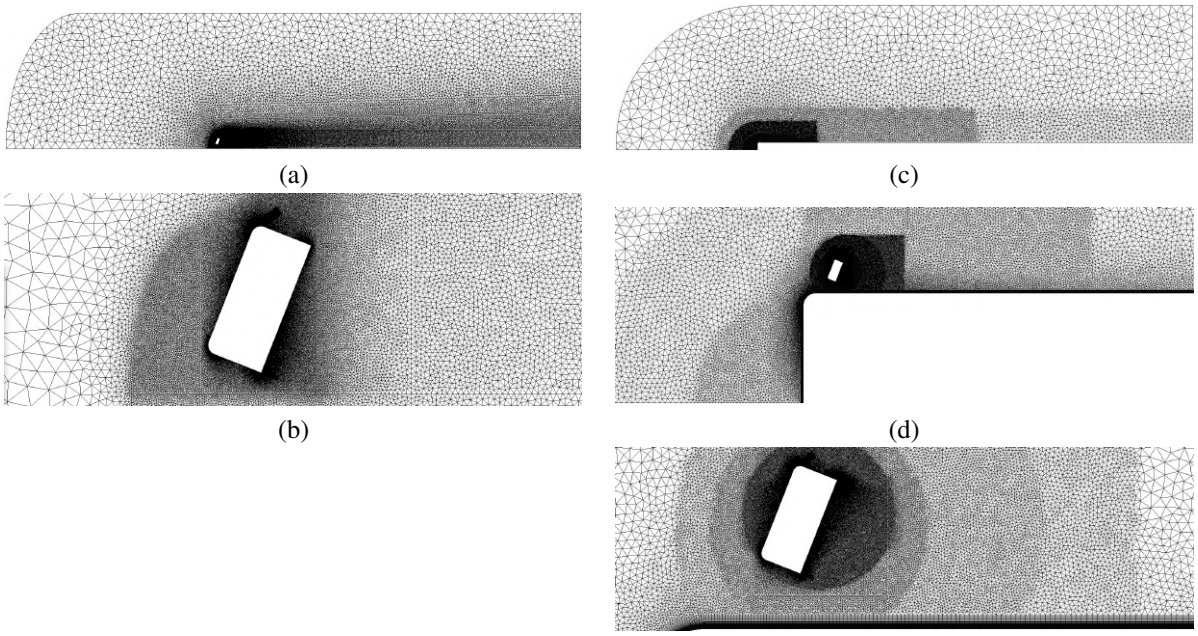

Table 4: Meshes with (left column) and without IE (right column) employed in the simulations. Full domain of the first mesh (a) and a its near-mirror region (b). Full domain of second mesh (c), details of the mesh close the truck (d) and the details of the mirror's vicinity (e). MO mesh adapted from Carvalho and da Silva (2021).

the spectral estimation, the data must be divided into multiple blocks Schmidt *et al.* (2017). This decreases estimation uncertainty but requires every event, specially the one with the lowest frequency, to occur multiple times in each one of these blocks of data. Handling these two conditions, every physical phenomenon of interest present within the flow is satisfactorily represented by the data series. However, if the difference between the lowest and highest frequencies is too substantial, a vast number of snapshots may be required,creating a considerable demand for computational effort or/and memory storage.

The SPOD output the modes by frequency and energy content. The number of modes depends on the number of blocks used to break the data series. These modes are distributed by decreasing order of their eigenvalues. A larger eigenvalue means that the physical structure represented by the mode have more energy (as measured by the selected inner product), and can have a significant impact in the flow dynamics. Moreover, these energetic structures can often be associated with the main flow features.

The chosen norm was the L2-norm weighted by an estimation of the local area surrounding each mesh node. According to Schmidt and Colonius (2020), this norm makes the SPOD modes of adequately discretized meshes to be independent of its structural details. It balances the impact of regions with different concentration of mesh nodes.

4. Results

The first configuration was simulated using a time step of 0.0002 seconds and 1,000 internal iterations. To save memory storage, the solution files were written with a sampling period five times greater than the simulation's time step.

In order to verify mesh convergence, a further refined mesh was utilized to validate the MO simulation. This second mesh was build using 93% more points, 196,128 in total, and 321,822 elements. The same was done for the IE mesh, giving a refined version with 270,524 points (50% bigger) and 398,418 interior elements.

As Tab. 5 and Fig. 6 shows, the time-averaged drag value of the MO simulations are very similar. The same can be affirmed with respect to their most energetic Strouhal numbers. This alignment means that this original mesh is fine enough, and, considering the method's limitations, can give satisfactory results. The IE simulation didn't achieve a similar agreement with its validation, as Fig. 6 and Tab. 5 displays. The difference between their time-averaged drag is of 3.74%. The instantaneous drag of the original IE reached two distinct behaviours; it started with periodic oscillations, then reached non-periodic fluctuations and ended up returning to the first behaviour.

To better analyze the vortex shedding dynamics of the flow-fields, snapshots of both original simulations were plotted in Fig. 7. These snapshots were extracted from the instants A to J from Fig. 6, and they contain contours of vorticity and static pressure. To facilitate the description of the wake's structure, the vortices of negative and positive vorticity are

Table 5: Time-averaged drag coefficient and most energetic drag peak of the MO (left) and IE (right) simulations. The MO values are adapted from Carvalho and da Silva (2021).

MO Simulation	Mean Drag Coefficient	Most Energetic Strouhal
Original	2.4721	0.1537
Validation	2.4739	0.1543

IE Simulation	Mean Drag Coefficient	Most Energetic Strouhal
Original	3.2451	0.1332
Validation	3.1280	0.1452

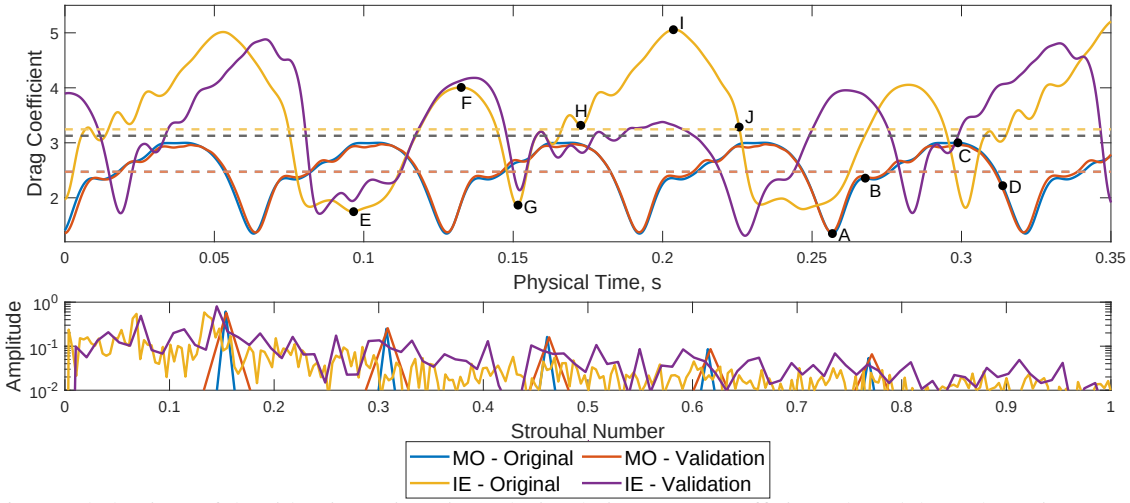

Figure 6: Drag behaviour of the side-view mirror in each simulation. Drag coefficient plotted throughout time (top) and in the Fast Fourier Transform's frequency domain (bottom). The MO curves are adapted from Carvalho and da Silva (2021).

called blue and red vortices, respectively. Their location and intensity greatly influences the pressure field and can be directly associated with the instantaneous drag value. When in contact with the mirror's surfaces, the low-pressure zones in the vortices' cores increase drag value.

In the wake of the MO geometry, a typical period starts with a blue vortex originated close to instant A. This vortex is smaller and detaches between instants B and C. After it separates, a red vortex immediately takes its place. While this transition is happening, the drag increases, but it faces a certain fluctuation due to this replacement. This second vortex is stronger and spawns near instant B, being fed by the fast fluid passing between the mirror and the wall. The pressure at its core reaches a minimum during instant C when it is at the imminence of separating from the mirror. Little after its detachment, during instant D, there are no significant sources of negative pressure in the mirror's rear face drag, making the drag rapidly decrease. After reaching its minimum, the drag starts rising again with the formation of another blue vortex, almost identical from the one created close to instant A, restarting the cycle.

Since the IE case presented the periodic behaviour for the majority of simulated time, this was the only part taken into consideration during the snapshot analysis. The cycle begins in the instant E when drag is in a local minimum. During this moment, little vortices are generated from both sides and struggle for dominance. The red one detaches first, interacts with the cabin's blue vorticity and later is absorbed by the larger red vortex of instant E. From instant E to F, the blue vortex grows and then detaches, giving room to another red vortex which generates a zone of substantially low pressure. The first peak of drag occurs when this red vortex is at its pinnacle. After it leaves the mirror's wall, the region with blue vorticity from the mirror's external side occupies its place. While this happens, the drag quickly decreases, providing a local minimum in the instant G. Later, the region of blue vorticity gets more intense and detaches. Similarly as in the MO simulation's wake, when the blue vortex is replaced by the red one, the drag coefficient faces some small instabilities. The red vortex starts growing dominant in the instant H. It expands further and gives origin to the highest drag peak of the whole period during instant I. Later, it detaches, making the drag quickly decreases again, producing another point of a local minimum. The cycle then restarts, return to a state similar to the one described in instant E.

In both geometries, the wake behaves with the following steps:

1. Pattern starts with a point of a minimum drag after a red vortex detaches;
2. Drag begins increasing with the growth of a blue vortex;
3. The blue vortex detaches and a red vortex quickly replaces it, making the drag coefficient continue to increase, but the instantaneous drag faces small instabilities during the transition;
4. Red vortex reaches its apex, making the drag reach a local maximum;

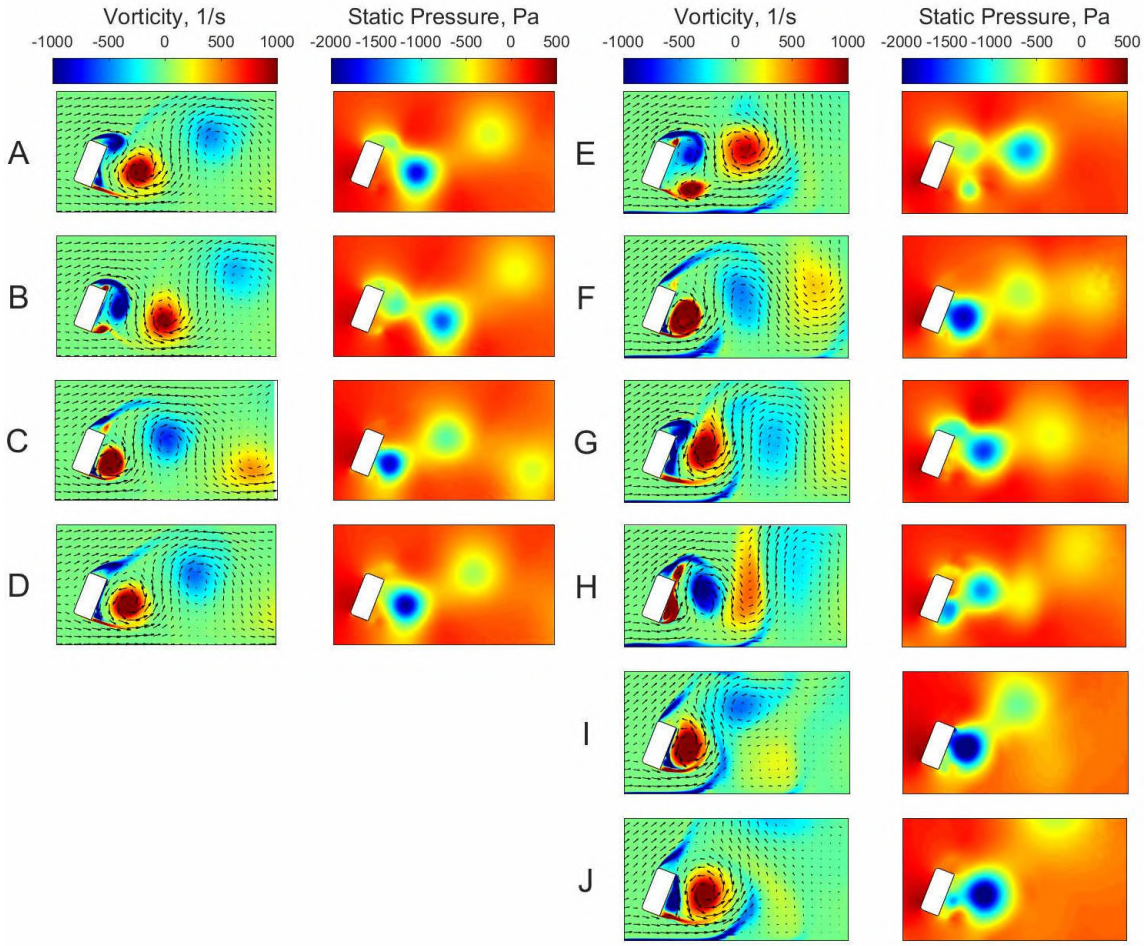

Figure 7: Contours of vorticity and of the difference between the freestream static pressure and the local static pressure. In the vorticity contours, the arrows displays the local velocity's magnitude and direction. The MO simulation is represented by the instants A-D (left) and the IE simulation by the instants E-J (right). The MO snapshots are adapted from Carvalho and da Silva (2021).

5. After its peak, the vortex detaches causing the drag to drop and reach a local minimum;

This process occurs distinctively twice within each period of the IE simulation, but with different vortices' strength and shape. These cycles demand less time in the MO simulation. The combination of slower vortex shedding and the existence of two distinct local peaks in instants F and I make the IE period more than two times bigger. Furthermore, the IE flow more intense wake sustains its pressure lower even during the interval between steps 1 and 5. This maintains the drag elevated and increases its time-average value.

Figure 8 shows periodograms containing the energy of each SPOD mode of velocity and pressure. The vertical dotted lines are selected frequencies where local peaks of energy occur. The real part of the most energetic SPOD mode in each one of these frequencies is shown in Fig. 9 together with their Strouhal number. Some similarities can be seen between the modes of the two simulations when their frequencies are close. However, the IE curves have smaller energy drop around its peaks, as if the flow-field had a broadband behaviour. Unfortunately, given the non-periodic behaviour of part of original IE simulation, the lack of definition in the peaks could be either due the presence of the aforementioned non-periodic oscillations or the real existence of multiple frequency structures being captured by the simulation.

A interesting region of this periodogram occurs close to drag's most energetic Strouhal ($Sr \approx 0.15$). The modes near this Strouhal shown in Fig. 9 indicates that the directions of the vortex shedding of the two simulations are different. The IE vortex shedding behaves as if it was subjected to a non-zero angle of attack. Furthermore, the contrast could suggest that the IE presence considerably modify the drag-related time-coherent structures.

Another interesting region occurs near the first harmonic of the most energetic Strouhal ($Sr \approx 0.30$). Differently from the $Sr \approx 0.15$ case, the IE simulation's modes in this frequency seem to be unaffected by a non-zero angle of attack. Moreover, for this higher frequency, the flow oscillation changes considerably in the near-wall region displayed at the bottom of each contour plot. Due to the difference in the boundary condition type, velocity oscillates more in this region in the MO simulation. This particular difference could indicate that the Euler wall of the MO case wields some influence

in the time-coherent drag-related structures.

The other two modes ($Sr \approx 0.07$ and $Sr \approx 0.205$) don't occur in the MO simulation, meaning that they could represent structures originated from mirror-truck interaction.

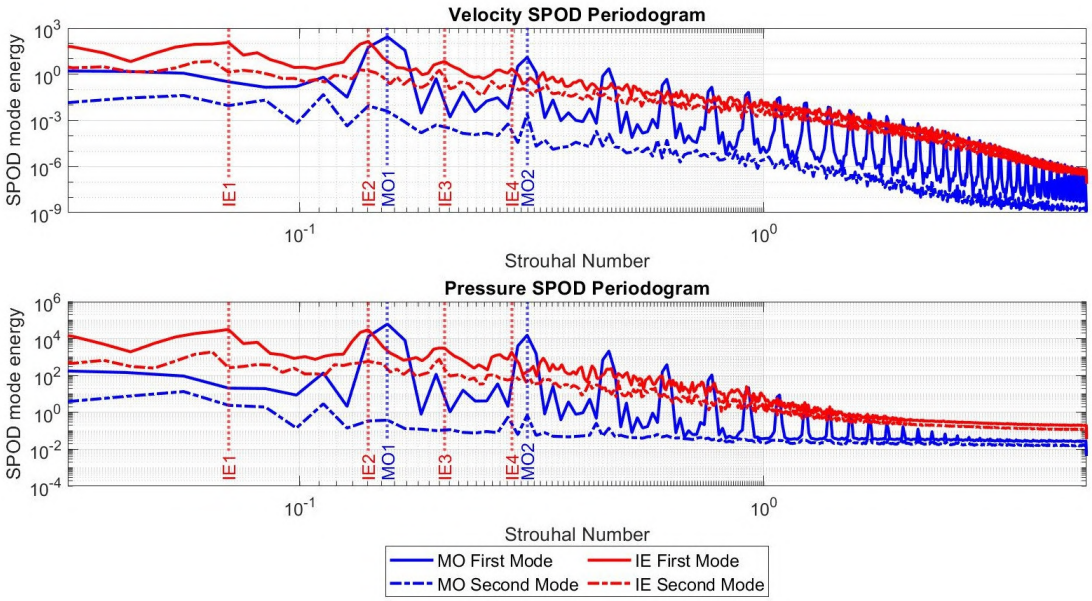

Figure 8: SPOD periodograms of velocity (top) and pressure (bottom). The continuous line represents their first mode and the dasheddotted line their second mode. The dotted lines indicate some selected peaks whose modes are plotted in Fig. 9. The MO curves are adapted from Carvalho and da Silva (2021).

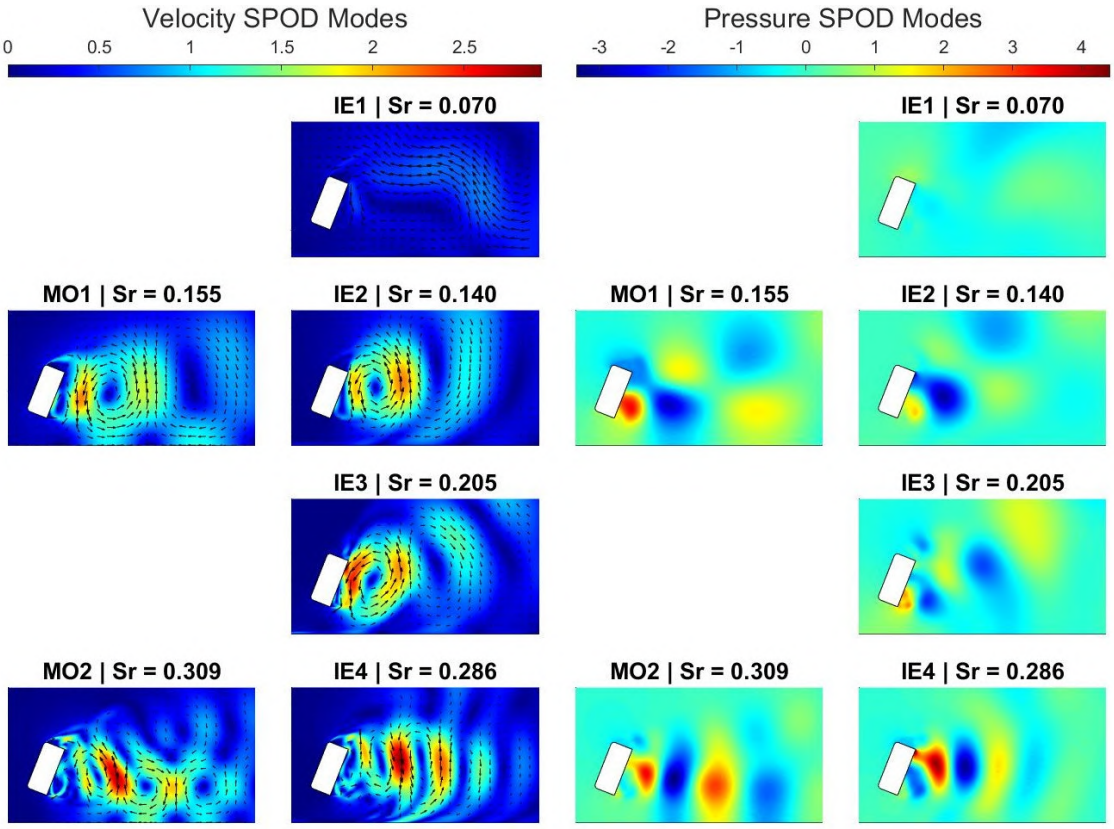

Figure 9: Contours of the real part of the most energetic SPOD modes of velocity and pressure of the MO (first and third columns) and IE (second and fourth columns) simulations. The velocity's arrows represent the mode's local magnitude and direction. The MO modes are adapted from Carvalho and da Silva (2021).

5. Conclusions

In this work, a generic geometry of a truck's side-view mirror was created. Implementing the regulatory requirements of this component, a reasonable position/inclination of this component was selected. This geometry was then converted in two 2D meshes, one considering the mirror alone close to a wall with free slip condition and another with a generic and simplified geometry of a cabin. These meshes were then employed in URANS-SST simulations. Their drag coefficient was analysed in the time and frequency domains. Additionally, instants of interest in the drag cycle were further investigated by the examination of snapshots of their vortex and pressure fields. Finally, this logic of selecting and inspecting snapshots was brought to the frequency domain through the analysis of SPOD modes.

The presented results showed differences and similarities between 2D simulations considering the installation effect or not. The substantial discrepancy between values of the time-averaged drag may suggest that this kind of force can not be directly extrapolated from one case to another.

The snapshot analysis revealed the process of generation, growth and detachment of vortices and how it is related to the drag's temporal behaviour. Moreover, it highlighted some similarities between the MO and IE simulations in how the vortex shedding impacts the instantaneous drag. One important consequence of these findings is the possibility of proposing changes to the geometry of the mirror that would lead to potential drag reductions. One example of such improvements could be produced by reducing the frontal top corner of the mirror's housing. This modification could potentially reduce the amount of recirculating fluid near the mirror's external side, a feature present in both IE and MO cases. Since the elimination of this recirculating structure would lead to a pressure increase in the external side's vicinity and a reduction in the mirror's effective transversal area, a decrease of the mean drag is expected.

The SPOD modes displayed substantial differences in the time-coherent structures related to drag. They revealed how the presence of the truck significantly altered the way flow interacts with the side-view mirror. Therefore, the results indicate that IE is an essential part of the drag analysis a truck's side-view mirror and significantly impacts the drag's time-averaged value and flow structures related to its main frequencies.

6. ACKNOWLEDGEMENTS

This study was financed in part by the Coordenação de Aperfeiçoamento de Pessoal de Nível Superior – Brasil (CAPES) – Finance Code 001.

7. REFERENCES

ANTT, 2020. "Registro Nacional dos Transportadores Rodoviários de Cargas (RNTRC)". Agência Nacional de Transportes Terrestres. 12 Oct 2020 <http://www.antt.gov.br>.

Bayraktar, I., Baysal, O. and Bayraktar, T., 2004. "Computational parametric study on external aerodynamics of heavy trucks". pp. 485–501.

Carvalho, E. and da Silva, A.F.C., 2021. "Adjoint-based aerodynamic optimization of a side-view mirror". *Proceedings of the 2021 SCITECH FORUM (Submitted)*.

CNT, 2018. "Plano CNT de Transporte e Logística 2018". Technical report, Confederação Nacional do Transporte, Brasília, Brazil.

Cooper, K.R., 2004. "Commercial vehicle aerodynamic drag reduction: Historical perspective as a guide". pp. 9–28.

Cresswell, M. and Hertz, P., 1992. "Aerodynamic drag implications of exterior truck mirrors". ISSN 0148-7191. doi: https://doi.org/10.4271/920204. URL `https://doi.org/10.4271/920204`.

EPE, 2019. "Brazilian Energy Balance 2019 Year 2018". Technical report, Empresa de Pesquisa Energética, Brasília, Brazil.

Frank, T. and Turney, J., 2016. "Aerodynamics of commercial vehicles". pp. 195–210.

Gao, Y., Liao, H., Burke, P. and Wei, Y., 2015. "Road transport energy consumption in the g7 and brics: 1973-2010". *International Journal of Global Energy Issues*, Vol. 38, p. 342. doi:10.1504/IJGEI.2015.070260.

Hjelm, L. and Bergqvist, B., 2009. "European truck aerodynamics – a comparison between conventional and coe truck aerodynamics and a look into future trends and possibilities". doi:10.1007/978-3-540-85070-0_45.

IBPT and Empresômetro, 2018. "Frota brasileira de veículos em circulação". Technical report, Instituto Brasileiro de Planejamento e Tributação and Empresômetro, Curitiba, Brazil.

IEA, 2019. "Data and statistics - Total Final Consumption (TFC) by sector, world 1990-2017". International Energy Agency. <https://www.iea.org/data-and-statistics>.

Jameson, A., Schmidt, W. and Turkel, E., 1981. "Numerical solution of the euler equations by finite volume methods using runge-kutta time stepping schemes". *AIAA Paper*, Vol. 81. doi:10.2514/6.1981-1259.

Manosalvas-Kjono, D., Economon, T., Palacios, F. and Jameson, A., 2014. "Finding computationally inexpensive methods to model the flow past heavy vehicles and the design of active flow control systems for drag reduction". *32nd AIAA Applied Aerodynamics Conference*. doi:10.2514/6.2014-2404.

Menter, F.R., 1994. "Two-equation eddy-viscosity turbulence models for engineering applications". *AIAA Journal*, Vol. 32, No. 8, pp. 1598–1605. doi:10.2514/3.12149. URL https://doi.org/10.2514/3.12149.

Palacios, F., Colonno, M., Aranake, A., Campos, A., Copeland, S., Economon, T., Lonkar, A., Lukaczyk, T., Taylor, T. and Alonso, J., 2013. "Stanford university unstructured (su2): An open-source integrated computational environment for multi-physics simulation and design". *51st AIAA Aerospace Sciences Meeting including the New Horizons Forum and Aerospace Exposition 2013*. doi:10.2514/6.2013-287.

Pope, S.B., 2000. *Turbulent-viscosity models*, Cambridge University Press, p. 358–386. doi:10.1017/CBO9780511840531.012.

Raut, G., Chaitanya, M., Upadhyay, A. and Kumar, M., 2015. "Impact of profile modifications and rear view mirror on aerodynamics and fuel economy of goods carrier". *Indian Journal of Science and Technology*, Vol. 8, p. 224. doi:10.17485/ijst/2015/v8iS2/61642.

Rodrigue, J., Comtois, C. and Slack, B., 2013. *The Geography of Transport Systems*. Routledge. ISBN 9780415822534. doi:https://doi.org/10.4324/9780203371183. URL https://books.google.com.br/books?id=crxiMgEACAAJ.

Roy, S. and Srinivasan, P., 2000. "External flow analysis of a truck for drag reduction". *SAE Technical Papers*. doi:10.4271/2000-01-3500.

Schmidt, O., Towne, A., Rigas, G., Colonius, T. and Brès, G., 2017. "Spectral analysis of jet turbulence". *Journal of Fluid Mechanics*, Vol. 855. doi:10.1017/jfm.2018.675.

Schmidt, O.T. and Colonius, T., 2020. "Guide to spectral proper orthogonal decomposition". *AIAA Journal*, Vol. 58, No. 3, pp. 1023–1033. doi:10.2514/1.J058809. URL https://doi.org/10.2514/1.J058809.

SINDIPEÇAS and ABIPEÇAS, 2019. "Relatório da Frota Circulante - edição de 2019". Technical report, Sindicato Nacional da Indústria de Componentes para Veículos Automotores and Associação Brasileira da Indústria de Autopeças, São Paulo, Brazil.

Smith, S., Younessi, K., Markstaller, M., Schlesinger, D., Bhatnagar, B., Smith, D., Banceu, B., Schoon, R., Sharma, V., Kachmarsky, M., Ghantae, S., Sorrels, M., Deedy, C., Clark, J., Yeakel, S., Laughlin, M., Seigler, C. and Diamond, S., 2007. "Test, Evaluation, and Demonstration of Pratical Devices/Systems to Reduce Aerodynamic Drag of Tractor/Semitrailer Combination Unit Truck". Technical report, Truck Manufacturers Association, Washington, DC. doi:10.2172/926158.

Towne, A., Schmidt, O.T. and Colonius, T., 2018. "Spectral proper orthogonal decomposition and its relationship to dynamic mode decomposition and resolvent analysis". *Journal of Fluid Mechanics*, Vol. 847, p. 821–867. doi:10.1017/jfm.2018.283.

Yao, H., Chroneer, Z. and Davidson, L., 2018. "Simplifications applied to simulation of turbulence induced by a side view mirror of a full-scale truck using des". ISSN 0148-7191. doi:https://doi.org/10.4271/2018-01-0708. URL https://doi.org/10.4271/2018-01-0708.

Yuce, M. and Kareem, D., 2016. "A numerical analysis of fluid flow around circular and square cylinders". *Journal - American Water Works Association*, Vol. 108, pp. E546 – E554. doi:10.5942/jawwa.2016.108.0141.

8. RESPONSIBILITY NOTICE

The authors are solely responsible for the printed material included in this paper.